Chin. Phys. Lett. **39**, 027401 (2022)

Superconductivity with a Violation of Pauli Limit and Evidences for Multigap in η-Carbide Type Ti_4Ir_2O

Bin-Bin Ruan(阮彬彬)[1,2*], Meng-Hu Zhou(周孟虎)[1,2], Qing-Song Yang(杨清松)[2,3], Ya-Dong Gu(谷亚东)[2,3], Ming-Wei Ma(马明伟)[2], Gen-Fu Chen(陈根富)[2,3], and Zhi-An Ren(任治安)[2,3*]

[1]*Songshan Lake Materials Laboratory, Dongguan 523808, China*
[2]*Institute of Physics and Beijing National Laboratory for Condensed Matter Physics, Chinese Academy of Sciences, Beijing 100190, China*
[3]*School of Physical Sciences, University of Chinese Academy of Sciences, Beijing 100049, China*

(Received 14 December 2021; accepted 12 January 2022; published online 29 January 2022)

We report the synthesis, crystal structure, and superconductivity of Ti_4Ir_2O. The title compound crystallizes in an η-carbide type structure of the space group $Fd\bar{3}m$ (No. 227), with lattice parameters $a = b = c = 11.6194(1)$ Å. The superconducting temperature T_c is found to be 5.1–5.7 K. Most surprisingly, Ti_4Ir_2O hosts an upper critical field of 16.45 T, which is far beyond the Pauli paramagnetic limit. Strong coupled superconductivity with evidences for multigap is revealed by the measurements of heat capacity and upper critical field. First-principles calculations suggest that the density of states near the Fermi level originates from the hybridization of Ti-3*d* and Ir-5*d* orbitals, and the effect of spin-orbit coupling on the Fermi surfaces is prominent. Large values of the Wilson ratio ($R_W \sim 3.9$), the Kadowaki–Woods ratio [$A/\gamma^2 \sim 9.0 \times 10^{-6}$ μΩ·cm/(mJ·mol^{-1}·K^{-1})^2], and the Sommerfeld coefficient ($\gamma = 33.74$ mJ·mol^{-1}·K^{-2}) all suggest strong electron correlations (similar to heavy fermion systems) in Ti_4Ir_2O. The violation of Pauli limit is possibly due to a combination of strong-coupled superconductivity and large spin-orbit scattering. With these intriguing behaviors, Ti_4Ir_2O serves as a candidate for unconventional superconductor.

DOI: 10.1088/0256-307X/39/2/027401

For their superior abilities to carry large currents, superconductors have been widely used to generate high magnetic fields at different settings, such as medical magnetic resonance imaging (MRI), maglevs, and particle accelerators.[1,2] However, applications to these uses have been limited to only a few superconducting compounds, primarily NbTi or Nb_3Sn.[3] Apart from the superconducting transition temperature (T_c), the critical current density, and the ductibility, one major limitation comes from the upper critical field (H_{c2}) in a type-Ⅱ superconductor.

At low temperatures, the Zeeman energy splitting (ΔE) is the key factor limiting H_{c2}. When the external magnetic field is large enough ($\geq \mu_0 H_P$), driving ΔE comparable with twice the superconducting energy gap, the Cooper pairs are broken. In a Bardeen–Cooper–Schrieffer (BCS) weak coupling scenario, the Pauli paramagnetic limit (or, Pauli limit for short) is expressed by $\mu_0 H_P = 1.86 \times T_c$ (T/K).

H_{c2} of most type-Ⅱ superconductors falls below H_P, regardless of the value of T_c.[4] However, a violation of the Pauli limit is often regarded as a side evidence for unconventional superconductivity, as in heavy fermions,[5] iron-based superconductors,[6] noncentrosymmetric superconductors,[7,8] and more recently, in $A_2Cr_3As_3$ (A = Na, K, Rb, Cs)[9–11] or magic-angle twisted trilayer graphene.[12]

In addition to unconventional superconductivity, large spin-orbit scattering,[13] strong electron-phonon coupling,[14] or a highly anisotropic structure[15] all tend to increase H_{c2}, pushing it beyond H_P. Nevertheless, superconductors with a violation of Pauli limit are still very rare.

In this study, we focus on a suboxide of the so-called η-carbide family, also known as the $E9_3$-type phases. The η-carbide type phase adopts a cubic crystal structure of the space group $Fd\bar{3}m$ (No. 227), which is derived from the Ti_2Ni type after small atoms, typically C, N, or O, take the interstitial sites. W_3Fe_3C, the first member in the family, was discovered in the 1950s.[16,17] Since then, a large number of carbides, nitrides, and oxides of the same structural family have been reported. Depending on different crystallographic sites the atoms take, there are four stoichiometries of η-carbide type phases, namely (T and T′ stand for transition metals, X = C, N, O): (a) $T_4T'_2X$, as in Mo_4Co_2C, Zr_4Re_2O;[17] (b) $T_3T'_3X$, as in W_3Fe_3C, Nb_3Cr_3N;[16] (c) $T_6T'_6X$, as in Mo_6Ni_6C;[18] (d) $T_8T'_4X$, as in Nb_8Zn_4C.[19] Although they have been discovered for more than half

*Corresponding author. Email: bbruan@mail.ustc.edu.cn; renzhian@iphy.ac.cn
© 2022 Chinese Physical Society and IOP Publishing Ltd

a century, reports on these phases mainly focus on their hardness,[20] the hydrogen-sorption,[21] or the catalytic abilities,[22] few of them have been examined for their electronic properties.

Ku *et al.* reported several η-carbide type superconductors in 1984,[23] including Ti_4Co_2O (T_c = 3.1 K), Zr_4Os_2O (T_c = 3.0 K), Nb_4Rh_2C (T_c = 8.9 K), etc. Recently, superconductivity in $Zr_4Rh_2O_{0.6}$[24] and $Nb_4Rh_2C_{1-\delta}$[25] was systematically studied. $Nb_4Rh_2C_{1-\delta}$ was found to host a large $\mu_0H_{c2}(0)$ of 28.5 T, violating the Pauli paramagnetic limit. This is not trivial since η-carbide type phases are not highly anisotropic in their crystal structures. Thus, strong electron correlations, or even unconventional superconductivity, can be expected in the superconductors of η-carbide type. However, evidences for these speculations are still absent.

In this Letter, we report the synthesis and a systematical study of superconductivity in Ti_4Ir_2O. Bulk superconductivity of T_c = 5.12 K is revealed by magnetic susceptibility and heat capacity measurements, confirming a previous report by Matthias *et al.* in 1963.[26] In that paper, superconductivity in "$Ti_{0.573}Ir_{0.287}O_{0.14}$" was reported without further details. Notice that such an early study needs reexamination. For example, superconductivity of T_c = 11.8 K in "$Zr_{0.61}Rh_{0.285}O_{0.105}$" reported in the same paper[26] was later ascribed to $CuAl_2$-type Zr_2Rh.[27] In addition, superconducting parameters of Ti_4Ir_2O are determined in our study, among which the $\mu_0H_{c2}(0)$ is 16.45 T, far above the Pauli limit (9.52 T). Moreover, the deviation of $\mu_0H_{c2}(T)$ from the Werthamer–Helfand–Hohenberg (WHH) theory, and the heat capacity in the superconducting state suggest a multigap nature. Large electron correlations in Ti_4Ir_2O are evidenced by both experimental results and first-principles calculations.

Methods. Polycrystalline samples of Ti_4Ir_2O were prepared by solid state reactions. Stoichiometric amount of titanium (powder, 99.99%), iridium (powder, 99.99%), and TiO_2 (powder, 99.95%) was mixed thoroughly, and then cold pressed into pellets. The pellets were placed in corundum crucibles, which were subsequently sealed into niobium tubes under purified argon. The niobium tubes were heated to 1800 K, held at the temperature for 20 hours, and then cooled down to room temperature by switching off the furnace. To avoid the oxidation of niobium tubes at high temperatures, heating treatments were carried out under an argon atmosphere. Grey and dense solid was obtained after opening the niobium tubes. No reaction between the samples and the niobium tubes was observed, and the weight losses after the reactions were negligible. We also performed reactions at lower temperatures or using arc-melting methods. However, these alternative methods did not produce single-phase samples (see the Supplementary Material).

Powder x-ray diffraction (XRD) measurements were carried out on a PAN-analytical x-ray diffractometer equipped with Cu K_α radiation at room temperature. The Rietveld refinement of the XRD results was performed with the GSAS package.[28] Temperature-dependent electrical resistivity and heat capacity of the sample were measured on a Quantum Design physical property measurement system (PPMS). DC magnetization was measured on a Quantum Design magnetic property measurement system (MPMS). Details for the physical property measurements can be found elsewhere.[29] All the data from the magnetization measurements were corrected based on the demagnetization factor, which was determined by the dimensions of the rectangular sample.[30]

First-principles calculations were carried out in the frame of the density functional theory (DFT), using the QUANTUM ESPRESSO (QE) package.[31–33] Generalized gradient approximation (GGA) exchange-correlation functionals of PBEsol[34] were selected, together with the projector augmented wave pseudopotentials from the PSLIBRARY package.[35] To take spin-orbit coupling (SOC) into account, we performed both the scalar-relativistic and fully relativistic calculations. Energy cutoffs were 100 Ry and 1000 Ry for the wavefunctions and the charge densities, respectively. A Monkhorst–Pack grid of 8^3 k-points was used for the self-consistent calculation, and a denser grid of 12^3 k-points was used to generate the density of states (DOS). Before the self-consistent calculation, the cell parameters, as well as the atomic positions, were fully relaxed starting from the experimental values, using the Broyden–Fletcher–Goldfarb–Shanno (BFGS) algorithm. The grid of k-mesh was checked for convergence. The Barder analysis was performed with the help of the CRITIC2 package.[36] Fermi surfaces were constructed on a superfine grid of 101^3 k-points, with the help of maximally localized Wannier functions (MLWFs) generated by the WANNIER90 code.[37,38]

Results. Figure 1 displays the powder XRD pattern of Ti_4Ir_2O collected at room temperature. We find that Ti_4Ir_2O crystallizes in an η-carbide type structure, which is of the space group $Fd\bar{3}m$ (No. 227). In the structure, Ti and Ir form a Ti_2Ni-type framework, where O takes the 16c (distorted octahedral) interstitial sites (see the inset of Fig. 1). We note that the inclusion of oxygen is key to stabilize the Ti_4Ir_2O phase, since no Ti_2Ni-type Ti_2Ir phase can be acquired (nor has it been reported in the Ti–Ir phase diagram[39]). The crucial roles of interstitial C, N, or O have been frequently observed in other η-carbide type phases, such as W_3Fe_3C,[17] Zr_4Pd_2N,[23]

or Zr_4Rh_2O.[24] Rietveld refinement was performed and the result is shown in Fig. 1, giving cell parameters $a = b = c = 11.6194(1)$ Å. The value is close to the reference one 11.620 Å.[26] The occupancy on each site is refined to be 1.0 (except for that of oxygen, which is fixed to 1). Detailed refined crystallographic parameters are summarized in Table 1. The fully relaxed cell parameters and atomic positions are also listed for comparison. Notice that the discrepancies between the DFT values and the experimental values are within 0.6%, and the inclusion of SOC has negligible effects on the crystallographic parameters.

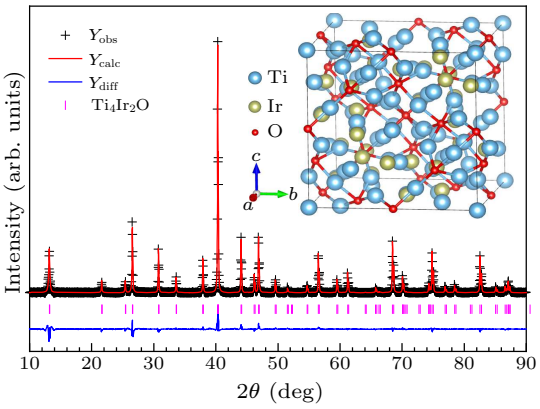

Fig. 1. Room-temperature XRD pattern of Ti_4Ir_2O and its Rietveld refinements. Y_{obs}, Y_{calc}, and Y_{diff} stand for the observed intensity, the calculated intensity, and the difference between them, respectively. The vertical bars indicate the Bragg positions for η-carbide type Ti_4Ir_2O. The conventional unit cell is shown as the inset.

Table 1. Crystallographic parameters of Ti_4Ir_2O from Rietveld refinement of room temperature XRD. Numbers in parentheses indicate the standard deviations in the last digit. Parameters from first-principles calculations are also listed for comparison. Here $R_p = 5.80\%$, $R_{wp} = 3.49\%$; $y_{Ti1} = z_{Ti1} = 0$, $y_{Ti2} = z_{Ti2} = 0.125$, $x_{Ir} = y_{Ir} = z_{Ir}$, $x_O = y_O = z_O$; U_{eq} is defined as one-third of trace of the orthogonalized U_{ij} tensor.

Space group		$Fd\bar{3}m$ (No. 227)		
a (Å)		11.6194(1)		
$a_{w/o-SOC}$ (Å)		11.5562		
$a_{with-SOC}$ (Å)		11.5531		
Atom (position)	x	U_{eq} (0.01 Å^2)	$x_{w/o-SOC}$	$x_{with-SOC}$
Ti1 (16c)	0	0.348(60)	0	0
Ti2 (48f)	0.4412(2)	0.065(25)	0.4428	0.4419
Ir (32e)	0.2145(0)	0.276(24)	0.2160	0.2159
O (16d)	0.5	0.633(150)	0.5	0.5

Superconductivity is evidenced in both resistivity and magnetization measurements, as shown in Fig. 2. At the normal state, Ti_4Ir_2O displays a metallic behavior, with the resistivity (ρ) decreasing upon cooling. The residual resistivity ratio ($RRR = \rho(300\,K)/\rho(6\,K) = 1.39$) is quite small, which is typical for a transition metal suboxide (for example, see Refs. [24,40]). The normal state $\rho(T)$ shows a convex feature (saturation) above 50 K. This can be explained with a parallel-resistor model, in which a strong electron-phonon coupling takes place (see, for instance, the A15 superconductors[41,42] and $SrPt_3P$[43]). Alternatively, it can be interpreted by an inter-band scattering, known as the Bloch–Grüneisen–Mott (BGM) mechanism.[29,44,45] The inset in Fig. 2 shows $\rho(T)$ below 70 K. We can find that the data below 35 K follow a Fermi liquid behavior:

$$\rho(T) = \rho_0 + AT^2, \tag{1}$$

giving $\rho_0 = 0.263\,m\Omega{\cdot}cm$, $A = 10.25\,n\Omega{\cdot}cm{\cdot}K^{-2}$. At lower temperatures, $\rho(T)$ starts to drop from 5.22 K (T_c^{onset}), reaching zero at 5.13 K (T_c^{zero}), indicating the occurrence of superconductivity. Such a sharp transition implies a superior homogeneity of our sample.

In Fig. 2(b), we show the DC magnetic susceptibility (χ) of Ti_4Ir_2O from 1.8 K to 8.0 K. The large diamagnetic signal in the zero-field cooling (ZFC) process confirms the bulk nature of the superconductivity. The field cooling (FC) gives a much smaller diamagnetism, suggesting a substantial pinning effect in the sample. T_c is determined to be 5.12 K from the first point to deviate from the normal state noises on the ZFC curve, which is in very good agreement with the value from $\rho(T)$. In the inset of Fig. 2(b), we show the temperature dependence of magnetization at the normal state, from which a Curie–Weiss behavior can be inferred.

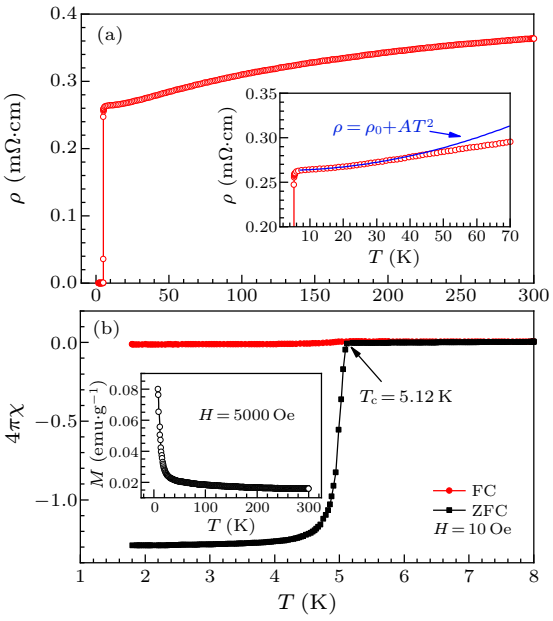

Fig. 2. (a) Temperature dependence of resistivity of Ti_4Ir_2O under zero magnetic field. Normal state data below 35 K can be described by Eq. (1), as shown in the inset. (b) Temperature dependence of DC magnetic susceptibility of Ti_4Ir_2O at low temperatures. Inset shows the temperature dependence of the normal state magnetization from 8 K to 300 K.

Figure 3(a) shows the superconducting transition under various magnetic fields. Clearly, the transition

is suppressed to lower temperatures when applying external fields. However, the suppression of T_c is very slow. For instance, under a magnetic field of 9 T, T_c is still above 2.5 K. Temperature dependence of the heat capacity (C_p) shows a distinct anomaly at low temperatures [Fig. 3(d)], which validates the bulk superconductivity again. T_c can be determined from the C_p/T–T curves based on an entropy balance method. At zero magnetic field, T_c determined from C_p is 5.12 K, which is in excellent agreement with the values from $\rho(T)$ and $\chi(T)$.

Results from $\rho(T)$ and C_p/T–T under various magnetic fields allow us to determine H_{c2} of Ti_4Ir_2O. In Fig. 3(f), the points from the $\rho(T)$ measurements are determined from the midpoints of the superconducting transitions, while points from C_p/T–T curves are determined using the method described above, error bars correspond to the transition width. The data from $\rho(T)$ and C_p/T–T agree well with each other, while the transition widths are larger in the C_p measurements. The Pauli paramagnetic limit for a superconductor with $T_c = 5.12$ K is ~9.52 T. However, as shown in Fig. 3(f), superconductivity still survives when the magnetic field is 12 T. This conclusively indicates a violation of Pauli limit in Ti_4Ir_2O.

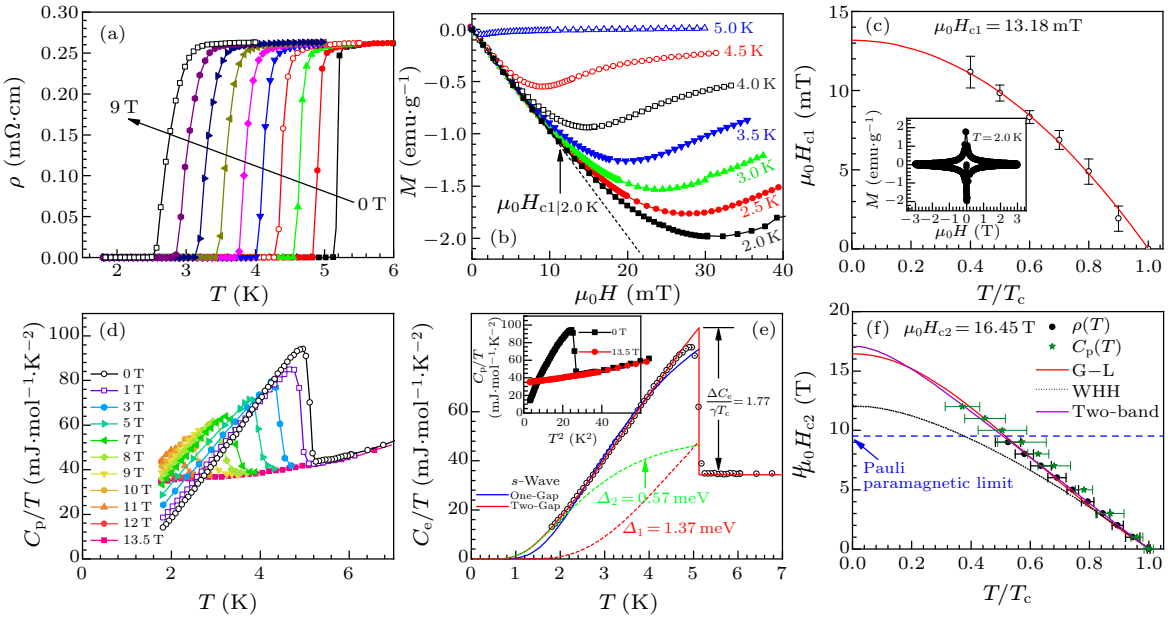

Fig. 3. (a) Superconducting transition on $\rho(T)$ under magnetic fields from 0 T to 9 T, the field increment between each curve is 1 T. (b) Isothermal magnetization under different temperatures. The dashed line shows the initial Meissner states. (c) Lower critical fields (H_{c1}) under different temperatures, and the fit according to the G–L relation. Inset shows the isothermal magnetization loop at 2.0 K. (d) Low temperature heat capacity under magnetic fields from 0 T to 13.5 T. (e) Electronic contribution of heat capacity at zero magnetic field. Solid curves show fits based on a one-gap s-wave model (blue), and a two-gap s-wave model (red). Contributions from the two gaps are displayed as dotted curves. (f) Upper critical fields (H_{c2}) under different temperatures, determined by $\rho(T)$ and $C_p(T)$. The fitting curves are based on the $\rho(T)$ data, according to the G–L (red), WHH (dotted), and two-band (purple) models, respectively. The value of $\mu_0 H_{c2}(0)$ is from the G–L fit.

The fit to H_{c2} is carried out using the WHH relation:[46]

$$\ln\left(\frac{1}{t}\right) = \left(\frac{1}{2} + \frac{i\lambda_{SO}}{4\gamma_w}\right)\psi\left(\frac{1}{2} + \frac{h + i\gamma_w + \lambda_{SO}/2}{2t}\right) + \left(\frac{1}{2} - \frac{i\lambda_{SO}}{4\gamma_w}\right)\psi\left(\frac{1}{2} + \frac{h - i\gamma_w + \lambda_{SO}/2}{2t}\right) - \psi\left(\frac{1}{2}\right), \quad (2)$$

where $t = T/T_c$ is the normalized temperature, $h = -(4/\pi^2)H_{c2}(T)/[T_c(dH_{c2}/dT)|_{T=T_c}]$ is the dimensionless magnetic field, and $\psi(x)$ is the Digamma function; $\gamma_w = (\alpha^2 h^2 - \lambda_{SO}^2/4)^{1/2}$, with α the Maki parameter, and λ_{SO} the parameter measuring the spin-orbit scattering. WHH fit of H_{c2} gives: $\alpha = 1.90$, $\lambda_{SO} = 14.05$. Such a large λ_{SO} means that there is little Pauli limiting effect in Ti_4Ir_2O, and the spin-orbit scattering dominates. However, as shown in Fig. 3(f), it fails to reproduce the H_{c2} data under magnetic fields beyond 7 T, yielding an underestimated $\mu_0 H_{c2}(0)$. In fact, $\lambda_{SO} \gg 1$ also implies that WHH theory, which assumes a small λ_{SO}, is unsuitable in our case. The failure of WHH fit comes from the linearity feature of the temperature dependence of H_{c2}. Such a deviation can be explained by multigap superconductivity, as observed in MgB_2,[47] 2H-$NbSe_2$,[48] iron-based superconductors,[6] and YRe_2SiC.[49] Indeed, the H_{c2} data is excellently reproduced by a two-band model developed by Gurevich,[50] as indicated by the purple line in Fig. 3(f). This is unsurprising because the

two-band model is based on many fitting parameters. To gain insights into the nature of the intra-band and inter-band scattering, detailed studies such as nuclear magnetic resonance (NMR) or muon spectroscopy are needed.

Alternatively, H_{c2} can also be fitted with the phenomenological Ginzburg–Landau (G–L) relation:

$$\mu_0 H_{c2}(T) = \mu_0 H_{c2}(0)\frac{1-(T/T_c)^2}{1+(T/T_c)^2}.$$

The G–L fit is also shown in Fig. 3(f), giving $\mu_0 H_{c2}(0) = 16.45\,\mathrm{T}$, which is much larger than the Pauli paramagnetic limit.

The isothermal magnetization (M–H) curves, shown in Fig. 3(b), give us knowledge about the lower critical field (H_{c1}). The magnetic field where the M–H curve starts to depart from the initial Meissner states (indicated by the dashed line) is determined as H_{c1}, which is plotted in Fig. 3(c). A G–L fit is carried out with the formula: $\mu_0 H_{c1}(T) = \mu_0 H_{c1}(0)[1-(T/T_c)^2]$, giving $\mu_0 H_{c1}(0) = 13.18\,\mathrm{mT}$. A full magnetization loop at 2.0 K is shown as the inset of Fig. 3(c), indicating type-Ⅱ superconductivity in Ti_4Ir_2O.

Based on the values of $H_{c1}(0)$ and $H_{c2}(0)$, a bunch of superconducting parameters, such as the G–L coherence length (ξ_{GL}), the penetration depth (λ_{GL}), the G–L parameter (κ_{GL}), and the thermodynamic field ($H_c(0)$) can be estimated. These parameters are summarized in Table 2. Details for calculating the parameters can be found in our previous study.[29] Notice that the value of κ_{GL} is close to the isostructural superconductor $Nb_4Rh_2C_{1-\delta}$,[25] and is far beyond $1/\sqrt{2}$, suggesting an extreme type-Ⅱ character.

Table 2. Normal state and superconducting parameters of Ti_4Ir_2O.

Parameter	Value	Notes
T_c^{onset} (K)	5.22	
T_c^{zero} (K)	5.13	From $\rho(T)$ (T_c ranges from 5.1 K to 5.7 K in samples prepared with different methods, see the Supplementary Material)
T_c^{mag} (K)	5.12	From $\chi(T)$
T_c^{HC} (K)	5.12	From $C_e(T)$
$\mu_0 H_{c1}(0)$ (mT)	13.18	From G–L fit
$\mu_0 H_{c2}(0)$ (T)	16.45	From G–L fit
$\mu_0 H_c(0)$ (T)	0.23	
ξ_{GL} (nm)	4.47	
λ_{GL} (nm)	236.1	
κ_{GL}	52.8	
γ (mJ·mol^{-1}·K^{-2})	33.74	
β (mJ·mol^{-1}·K^{-4})	0.265	
Θ_D (K)	372	
λ_{ep}	0.61	
$\Delta C_e/\gamma T_c$	1.77	
$\Delta_1/k_B T_c$	3.10	
$\Delta_2/k_B T_c$	1.29	
$N(E_F)$ (eV^{-1} per f.u.)	8.83	Experimental value deduced from γ
$N'(E_F)$ (eV^{-1} per f.u.)	7.26	Theoretical value from DFT calculation with SOC

Inset of Fig. 3(e) shows the heat capacity under zero field and under a field of 13.5 T, which totally suppress the superconducting transition above 1.8 K. The normal state data can be fitted with the Debye model: $C_p(T) = \gamma T + \beta T^3 + \delta T^5$, in which the three terms are the electronic contribution to the heat capacity (C_e), the harmonic phonon contribution, and the anharmonic phonon contribution, respectively. The fitting parameters are: $\gamma = 33.74\,\mathrm{mJ{\cdot}mol^{-1}{\cdot}K^{-2}}$, $\beta = 0.265\,\mathrm{mJ{\cdot}mol^{-1}{\cdot}K^{-4}}$, and $\delta = 2.53\,\mu\mathrm{J{\cdot}mol^{-1}{\cdot}K^{-6}}$. Debye temperature ($\Theta_D$) can be obtained by

$$\Theta_D = \left(\frac{12\pi^4 NR}{5\beta}\right)^{1/3}, \tag{3}$$

where N is the number of atoms per formula and R is the ideal gas constant. From Eq. (3) we obtain $\Theta_D = 372\,\mathrm{K}$.

According to the McMillan relation,[51] the electron-phonon coupling strength (λ_{ep}) can be expressed as

$$\lambda_{ep} = \frac{1.04+\mu^*\ln(\Theta_D/1.45T_c)}{(1-0.62\mu^*)\ln(\Theta_D/1.45T_c)-1.04}. \tag{4}$$

Setting the Coulomb screening parameter μ^* to 0.13, a typical value for intermetallics, we obtain $\lambda_{ep} = 0.61$, suggesting moderate coupling in Ti_4Ir_2O. The density of states (DOS) at the Fermi level (E_F) is calculated with $N(E_F) = 3\gamma/[\pi^2 k_B^2(1+\lambda_{ep})] = 8.83\,\mathrm{eV^{-1}}$ per formula unit (f.u.).

C_e gives us more insights about the nature of the superconductivity. To exclude the contribution of any possible impurities, C_e is obtained by subtracting

$C_p|_{\mu_0 H=0} + \gamma$ on $C_p|_{\mu_0 H=13.5T}$. The result is shown in Fig. 3(e). At the superconducting state, C_e quickly approaches zero, indicating a nodeless feature of the superconducting gap. Therefore, fit to the C_e is carried out based on isotropic s-wave models. However, a one-gap s-wave model fails to describe C_e at the superconducting state. Entropy balance at the superconducting transition is not fulfilled either. On the other hand, a two-gap s-wave model perfectly describes the C_e behavior, while maintaining the entropy balance. The two superconducting gaps are determined to be $\Delta_1 = 1.37\,\text{meV}$ and $\Delta_2 = 0.57\,\text{meV}$. Notice that the larger one is above the BCS weak coupling value ($\Delta_1/k_B T_c = 3.10 > 1.76$). This again indicates an enhanced electron-phonon coupling in Ti_4Ir_2O, which is further evidenced by the large C_e jump at T_c ($\Delta C_e/\gamma T_c = 1.77$).

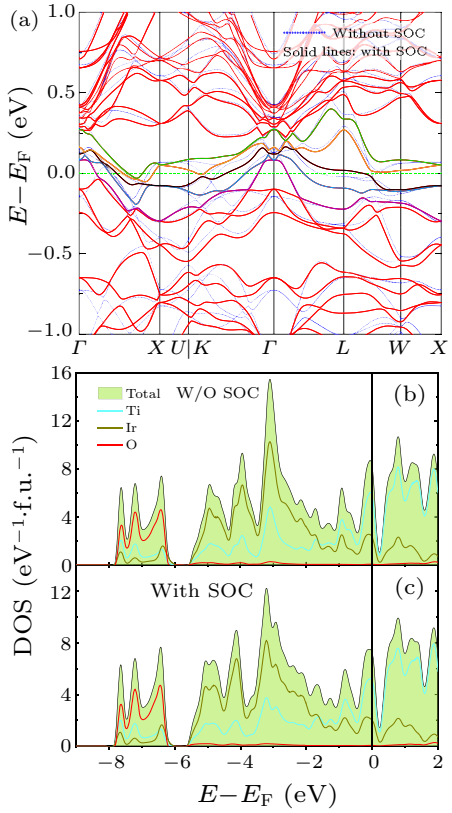

Fig. 4. (a) Electronic band structures of Ti_4Ir_2O from DFT calculation. Dotted lines show the results without SOC, while the SOC results are shown as solid lines. Solid lines in colors other than red indicate the bands crossing the Fermi level. (b) Projected DOS without SOC. (c) Projected DOS with SOC.

Results from the first principles calculation are shown in Fig. 4, with electronic band structures in Fig. 4(a) and DOS in Figs. 4(b) and 4(c). Both the scalar relativistic (w/o SOC) and the fully relativistic (with SOC) results are shown. In both cases, there are five bands crossing the Fermi level, consistent with the metallic nature of Ti_4Ir_2O. The existence of multiple bands crossing E_F also makes multigap superconductivity plausible. Notice that the energy dispersion near E_F is dramatically changed when SOC is turned on. For example, band splitting occurs along the Γ–X, Γ–K, and L–W lines. This makes the Fermi surface topology very different when considering SOC (see Fig. S5). Most absorbingly, nesting between the electron-like and hole-like pockets becomes prominent when SOC is turned on.

The Barder analysis was based on the converged charge densities, resulting in a valence configuration of $Ti_4^{1.32+}Ir_2^{1.94-}O^{1.40-}$. This means charge transferring from Ti to Ir and O. The charge density and electron localization function (ELF) maps are shown in Fig. S4, from which ionic Ti–O bonds and metallic Ti–Ir bonds can be identified.

From the projected DOS, shown in Figs. 4(b) and 4(c), we note the states from O are absent near E_F. While they hybridize with states from Ti at ~ -5.6 to $-2\,\text{eV}$, indicating the formation of Ti–O bonds. DOS at E_F is slightly lowered with SOC, giving a theoretical $N'(E_F) = 7.26\,\text{eV}^{-1}$ per f.u. This value is comparable with the one calculated from γ. The slightly enhancement of experimental $N(E_F)$ is possibly due to the electron-electron correlations. Notice that E_F locates near a pronounced peak of DOS, which arises from the relatively flat energy dispersion of the bands near E_F. After the projection to each atomic orbital, we find that DOS at E_F originates mainly from the Ti-3d orbitals, with minor contributions from the Ir-5d components.

Discussion and Conclusion. First we would like to discuss the stoichiometry of Ti_4Ir_2O, because η-carbide type phases frequently host vacancies on the interstitial sites.[24,25] According to the preparation procedure and the XRD results, however, the oxygen vacancies should be very close to zero. On the other hand, there should be a tiny amount of oxygen vacancies, since samples prepared at 1250 K were found to host smaller lattices and an enhanced T_c of 5.7 K (see the Supplementary Material). In η-carbide type suboxides, the lattice shrinks when more oxygen is incorporated, as observed in $Zr_4Rh_2O_{0.6}$.[24] This means that the oxygen contents in the 5.7 K samples are larger. The change of T_c should be attributed to the slight non-stoichiometry of Ti_4Ir_2O, given that DOS has a steep slope at E_F. In other words, a small amount of electron doping can dramatically change the value of $N(E_F)$. For example, $N(E_F)$ would be reduced to $6.80\,\text{eV}^{-1}$ per f.u. if 10% oxygen vacancies were introduced (assuming a rigid band model). The evolution of T_c upon vacancies requires detailed doping studies in the future.

Next we focus on the origin of the large H_{c2}. One possible cause of the enhancement of H_{c2} is the spin-triplet component in the order parameter, which can be induced by non-

centrosymmetric crystal structures.[7,8] However, this should not be the case since Ti_4Ir_2O hosts a centrosymmetric crystal structure. Another possibility of enhancement due to anisotropy, as observed in many low-dimensional superconductors, such as $Li_{0.9}Mo_6O_{17}$,[52] $LaO_{0.5}F_{0.5}BiS_2$,[15] La_2IRu_2,[53] and $K_2Mo_3As_3$,[54] is also ruled out. Because both the crystal structure and the Fermi surfaces (see Fig. S5) are clearly three-dimensional.

In heavy fermion superconductors, a reduction of g factor can cause a violation of the Pauli limit.[55] To see whether there is a strong correlation, a fit to the normal state magnetization data is carried out based on $\chi(T) = \chi_0 + C/(T-\theta)$, giving a temperature-independent term of $\chi_0 = 1.73 \times 10^{-3}\,\mathrm{emu{\cdot}mol^{-1}}$. After subtracting the core diamagnetic contributions from Ti^{4+}, Ir^{4+}, and O^{2-}, we obtain an estimation of the Pauli paramagnetic susceptibility $\chi_P \sim 1.84 \times 10^{-3}\,\mathrm{emu{\cdot}mol^{-1}}$. Therefore, the Wilson ratio $R_W = \pi^2 k_B^2 \chi_P/(3\gamma\mu_B^2) \sim 3.9$. Such a large R_W indicates the existence of strong electron correlation and/or an underlying magnetic order.[56,57] The strong electron correlation is further evidenced by the Kadowaki–Woods ratio $A/\gamma^2 = 9.0\times 10^{-6}\,\mu\Omega{\cdot}\mathrm{cm}/(\mathrm{mJ{\cdot}mol^{-1}{\cdot}K^{-1}})^2$, which is comparable with those in heavy fermion systems (for instance, $1.0 \times 10^{-5}\,\mu\Omega{\cdot}\mathrm{cm}/(\mathrm{mJ{\cdot}mol^{-1}{\cdot}K^{-1}})^2$ for UPt_3[5] and $CeCu_2Si_2$[58]). It is also probably the cause for the enhancement of γ compared with the theoretical value. The strong correlation might cause an enhancement of the electronic effective mass (m^*) and a reduction of g factor, which would result in a large H_{c2}. However, there is currently no clear experimental evidence for such an assumption. Further studies are needed to elucidate this issue.

Finally, since the Pauli limit is based on the BCS weak coupling gap value of $1.76k_BT_c$, a strong coupling can also enhance it. In our case, $\Delta_1/k_BT_c = 3.10$ is indeed beyond the BCS weak coupling limit. However, superconductors with similar coupling strength, such as the A15 compounds[41,42] or $SrPt_3P$,[43] do not necessarily host a large H_{c2}. The violation of Pauli limit in Ti_4Ir_2O is possibly due to a combination of the strong-coupled superconductivity and the spin-orbit scattering, while unconventional superconductivity cannot be excluded.

To summarize, we have reported a detailed investigation of superconductivity in Ti_4Ir_2O. As a strong-coupled superconductor with $T_c = 5.1 \sim 5.7\,\mathrm{K}$, Ti_4Ir_2O exhibits many intriguing properties. It has a large $\mu_0 H_{c2}(0)$ of 16.45 T, which is beyond the Pauli paramagnetic limit. A multigap superconductivity is suggested by the temperature dependence of H_{c2}, the heat capacity measurements, and the DFT calculations. Moreover, a strong electron correlation in Ti_4Ir_2O, which is comparable with typical heavy fermion superconductors, is revealed by the large values of the Wilson ratio and the Kadowaki–Woods ratio, as well as the relatively large Sommerfeld coefficient (γ). These results make Ti_4Ir_2O a rare example to study the interplay between strong electron correlation and multigap superconductivity. We note that these results also strongly suggest unconventional superconductivity. Questions like whether there are spin fluctuations or a direct observation of the multigap feature through spectroscopy methods are still open, calling for further studies. Given the fact that there are numerous η-carbide type compounds, most of which are not systematically investigated for their transport properties, detailed studies in this structural family may flourish in the near future.

Note. During the preparation of the manuscript, we note an independent report (published in November 2021) of superconductivity in Ti_4Ir_2O by Ma *et al.*[59] The superconducting parameters determined there are in agreement fairly well with ours.

Acknowledgments. This work was supported by the National Natural Science Foundation of China (Grant Nos. 12074414 and 11774402), the National Key Research and Development of China (Grant No. 2018YFA0704200), and the Strategic Priority Research Program of Chinese Academy of Sciences (Grant No. XDB25000000).

References

[1] Gurevich A 2011 *Nat. Mater.* **10** 255
[2] Hahn S, Kim K, Kim K, Hu X, Painter T, Dixon I, Kim S, Bhattarai K R, Noguchi S, Jaroszynski J and Larbalestier D C 2019 *Nature* **570** 496
[3] Stewart G 2015 *Physica C* **514** 28
[4] Poole C K, Farach H A and Creswick R J 1999 *Handbook of Superconductivity* (Amsterdam: Elsevier)
[5] Stewart G, Fisk Z, Willis J and Smith J 1984 *Phys. Rev. Lett.* **52** 679
[6] Tao Q, shen J Q, Li L J et al 2009 *Chin. Phys. Lett.* **26** 097401
[7] Bauer E, Hilscher G, Michor H, Paul C, Scheidt E, Gribanov A, Seropegin Y, Noel H, Sigrist M and Rogl P 2004 *Phys. Rev. Lett.* **92** 027003
[8] Gupta R, Ying T, Qi Y, Hosono H and Khasanov R 2021 *Phys. Rev. B* **103** 174511
[9] Bao J K, Liu J Y, Ma C W, Meng Z H, Tang Z T, Sun Y L, Zhai H F, Jiang H, Bai H, Feng C M *et al.* 2015 *Phys. Rev. X* **5** 011013
[10] Zhi H, Imai T, Ning F, Bao J K and Cao G H 2015 *Phys. Rev. Lett.* **114** 147004
[11] Tang Z T, Bao J K, Liu Y, Sun Y L, Ablimit A, Zhai H F, Jiang H, Feng C M, Xu Z A and Cao G H 2015 *Phys. Rev. B* **91** 020506
[12] Cao Y, Park J M, Watanabe K, Taniguchi T and Jarillo-Herrero P 2021 *Nature* **595** 526
[13] Lu Y, Takayama T, Bangura A F, Katsura Y, Hashizume D and Takagi H 2014 *J. Phys. Soc. Jpn.* **83** 023702
[14] Okuda K, Kitagawa M, Sakakibara T and Date M 1980 *J. Phys. Soc. Jpn.* **48** 2157
[15] Chan Y C, Yip K Y, Cheung Y W, Chan Y T, Niu Q, Kajitani J, Higashinaka R, Matsuda T D, Yanase Y, Aoki Y,

Lai K T and Goh S K 2018 *Phys. Rev. B* **97** 104509
[16] Taylor A and Sachs K 1952 *Nature* **169** 411
[17] Kuo K 1953 *Acta Metall.* **1** 301
[18] Newsam J, Jacobson A, McCandlish L and Polizzotti R 1988 *J. Solid State Chem.* **75** 296
[19] Jeitschko W, Holleck H, Nowotny H and Benesovsky F 1964 *Monatsh. Chem.* **95** 1004
[20] Dubrovinskaia N, Dubrovinsky L, Saxena S, Selleby M and Sundman B 1999 *J. Alloys Compd.* **285** 242
[21] Zavalii I, Verbovytskyi Y, Berezovets V, Shtender V, Pecharsky V and Lyutyi P 2017 *Mater. Sci.* **53** 306
[22] Nagai M, Zahidul A M and Matsuda K 2006 *Appl. Catal. A* **313** 137
[23] Ku H and Johnston D 1984 *Chin. J. Phys.* **22** 59
[24] Ma K, Lago J and von Rohr F O 2019 *J. Alloys Compd.* **796** 287
[25] Ma K, Gornicka K, Lefèvre R, Yang Y, Rønnow H M, Jeschke H O, Klimczuk T and von Rohr F O 2021 *ACS Materials Au* **1** 55
[26] Matthias B, Geballe T and Compton V 1963 *Rev. Mod. Phys.* **35** 1
[27] Zegler S 1965 *J. Phys. Chem. Solids* **26** 1347
[28] Toby B 2001 *J. Appl. Crystallogr.* **34** 210
[29] Ruan B B, Yang Q S, Zhou M H, Chen G F and Ren Z A 2021 *J. Alloys Compd.* **868** 159230
[30] Prozorov R and Kogan V G 2018 *Phys. Rev. Appl.* **10** 014030
[31] Giannozzi P, Baroni S, Bonini N, Calandra M, Car R, Cavazzoni C, Ceresoli D, Chiarotti G L, Cococcioni M, Dabo I, Dal C A, de Gironcoli S, Fabris S, Fratesi G, Gebauer R, Gerstmann U, Gougoussis C, Kokalj A, Lazzeri M, Martin-Samos L, Marzari N, Mauri F, Mazzarello R, Paolini S, Pasquarello A, Paulatto L, Sbraccia C, Scandolo S, Sclauzero G, Seitsonen A P, Smogunov A, Umari P and Wentzcovitch R M 2009 *J. Phys.: Condens. Matter* **21** 395502
[32] Giannozzi P, Andreussi O, Brumme T, Bunau O, Nardelli M B, Calandra M, Car R, Cavazzoni C, Ceresoli D, Cococcioni M, Colonna N, Carnimeo I, Corso A D, de Gironcoli S, Delugas P, DiStasio R A, Ferretti A, Floris A, Fratesi G, Fugallo G, Gebauer R, Gerstmann U, Giustino F, Gorni T, Jia J, Kawamura M, Ko H Y, Kokalj A, Küçükbenli E, Lazzeri M, Marsili M, Marzari N, Mauri F, Nguyen N L, Nguyen H V, Otero-de-la-Roza A, Paulatto L, Poncé S, Rocca D, Sabatini R, Santra B, Schlipf M, Seitsonen A P, Smogunov A, Timrov I, Thonhauser T, Umari P, Vast N, Wu X and Baroni S 2017 *J. Phys.: Condens. Matter* **29** 465901
[33] Giannozzi P, Baseggio O, Bonfa P, Brunato D, Car R, Carnimeo I, Cavazzoni C, de Gironcoli S, Delugas P, Ruffino F F, Ferretti A, Marzari N, Timrov I, Urru A and Baroni S 2020 *J. Chem. Phys.* **152** 154105
[34] Perdew J P, Ruzsinszky A, Csonka G I, Vydrov O A, Scuseria G E, Constantin L A, Zhou X and Burke K 2008 *Phys. Rev. Lett.* **100** 136406
[35] Dal C A 2014 *Comput. Mater. Sci.* **95** 337
[36] Otero-de-la-Roza A, Johnson E R and Luana V 2014 *Comput. Phys. Commun.* **185** 1007
[37] Fuhr J D, Roura-Bas P and Aligia A A 2021 *Phys. Rev. B* **103** 035126
[38] Pizzi G, Vitale V, Arita R, Bluegel S, Freimuth F, Geranton G, Gibertini M, Gresch D, Johnson C, Koretsune T, Ibanez-Azpiroz J, Lee H, Lihm J M, Marchand D, Marrazzo A, Mokrousov Y, Mustafa I J, Nohara Y, Nomura Y, Paulatto L, Ponce S, Ponweiser T, Qiao J, Thoele F, Tsirkin S S, Wierzbowska M, Marzari N, Vanderbilt D, Souza I, Mostofi A A and Yates J R 2020 *J. Phys.: Condens. Matter* **32** 165902
[39] Okamoto H, Massalski T *et al.* 1990 *Binary Alloy Phase Diagrams* (Materials Park, OH: ASM International)
[40] Xu C, Wang H, Tian H, Shi Y, Li Z A, Xiao R, Shi H, Yang H and Li J 2021 *Chin. Phys. B* **30** 077403
[41] Carbotte J 1990 *Rev. Mod. Phys.* **62** 1027
[42] Fisk Z and Webb G 1976 *Phys. Rev. Lett.* **36** 1084
[43] Takayama T, Kuwano K, Hirai D, Katsura Y, Yamamoto A and Takagi H 2012 *Phys. Rev. Lett.* **108** 237001
[44] Mott N F, Jones H, Jones H and Jones H 1958 *The Theory of the Properties of Metals and Alloys* (Courier Dover Publications)
[45] Mott N F 1964 *Adv. Phys.* **13** 325
[46] Werthamer N, Helfand E and PC H 1966 *Phys. Rev.* **147** 288
[47] Bud'ko S, Petrovic C, Lapertot G, Cunningham C, Canfield P, Jung M and Lacerda A 2001 *Phys. Rev. B* **63** 220503
[48] Suderow H, Tissen V, Brison J, Martínez J and Vieira S 2005 *Phys. Rev. Lett.* **95** 117006
[49] De Faria L R, Ferreira P P, Correa L E, Eleno L T, Torikachvili M S and Machado A J 2021 *Supercond. Sci. Technol.* **34** 065010
[50] Gurevich A 2003 *Phys. Rev. B* **67** 184515
[51] McMillan W L 1968 *Phys. Rev.* **167** 331
[52] Mercure J F, Bangura A F, Xu X, Wakeham N, Carrington A, Walmsley P, Greenblatt M and Hussey N E 2012 *Phys. Rev. Lett.* **108** 187003
[53] Ishikawa H, Wedig U, Nuss J, Kremer R K, Dinnebier R, Blankenhorn M, Pakdaman M, Matsumoto Y, Takayama T, Kitagawa K and Takagi H 2019 *Inorg. Chem.* **58** 12888
[54] Mu Q G, Ruan B B, Zhao K, Pan B J, Liu T, Shan L, Chen G F and Ren Z A 2018 *Sci. Bull.* **63** 952
[55] Altarawneh M, Harrison N, Li G, Balicas L, Tobash P, Ronning F and Bauer E 2012 *Phys. Rev. Lett.* **108** 066407
[56] Anand V K, Adroja D T and Hillier A D 2012 *Phys. Rev. B* **85** 014418
[57] Tong P, Sun Y P, Zhu X B and Song W H 2006 *Phys. Rev. B* **73** 245106
[58] Steglich F, Aarts J, Bredl C, Lieke W, Meschede D, Franz W and Schafer H 1979 *Phys. Rev. Lett.* **43** 1892
[59] Ma K, Lefèvre R, Gornicka K, Jeschke H O, Zhang X, Guguchia Z, Klimczuk T and von Rohr F O 2021 *Chem. Mater.* **33** 8722

Supplementary Material for "Superconductivity with a Violation of Pauli Limit and Evidences for Multigap in η-Carbide type Ti_4Ir_2O"

Bin-Bin Ruan(阮彬彬)[1,2*], Meng-Hu Zhou(周孟虎)[1,2], Qing-Song Yang(杨清松)[2,3], Ya-Dong Gu(谷亚东)[2,3], Ming-Wei Ma(马明伟)[2], Gen-Fu Chen(陈根富)[2,3], and Zhi-An Ren(任治安)[2,3*]

[1]Songshan Lake Materials Laboratory, Dongguan 523808, China
[2]Institute of Physics and Beijing National Laboratory for Condensed Matter Physics, Chinese Academy of Sciences, Beijing 100190, China
[3]School of Physical Sciences, University of Chinese Academy of Sciences, Beijing 100049, China
[*]Corresponding authors. E-mail: bbruan@mail.ustc.edu.cn; renzhian@iphy.ac.cn

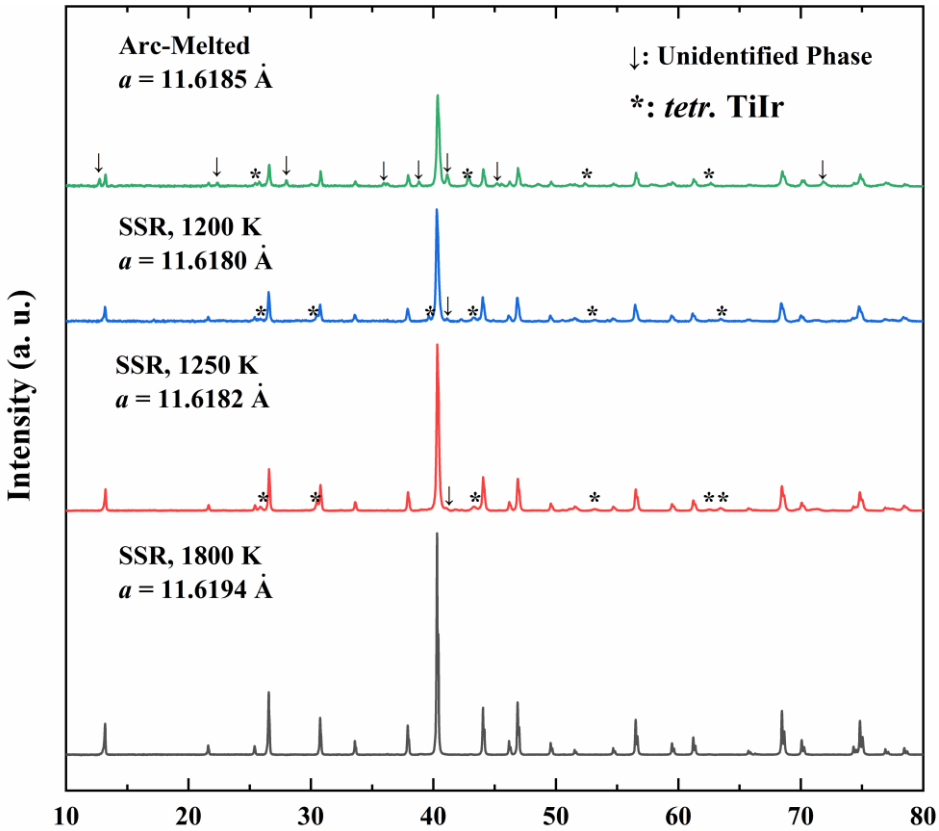

Figure S1: Representative XRD patterns of Ti_4Ir_2O samples prepared with different methods. From bottom to top: SSR (Solid state reaction) at 1800 K, SSR at 1250 K, SSR at 1200 K, and arc-melted samples. SSR at 1800 K produced single-phase sample, while the other three methods produced multi-phase samples. The lattice parameter *a* is slightly different too. *Tetr.* TiIr stands for tetragonal TiIr (space group *P*4/*mmm*). "↓" indicates an unidentified phase.

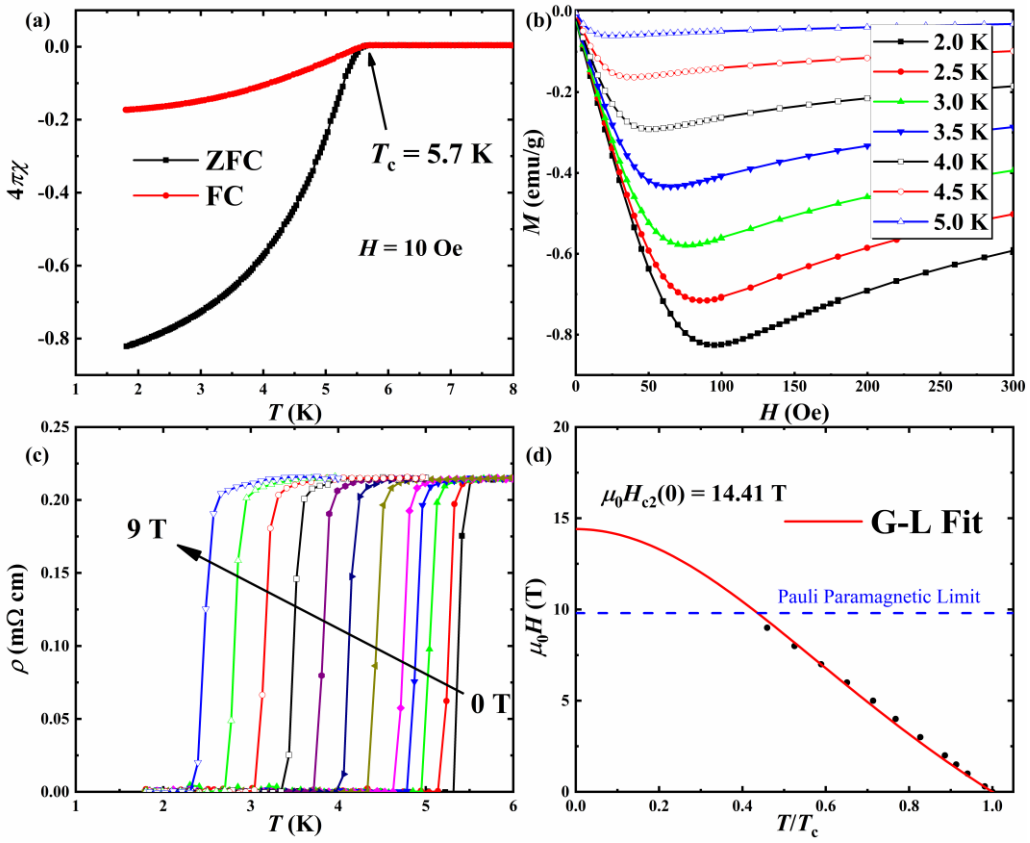

Figure S2: Electrical and magnetic properties of Ti_4Ir_2O prepared by SSR at 1200 K. Notice that although T_c of this sample is somewhat higher than the one shown in the main text, the transition width is larger, and the upper critical field is lower (but still above the Pauli limit), indicating a less good sample quality. (a) DC magnetic susceptibility under 10 Oe from 1.8 K to 8 K. (b) Isothermal magnetization curves at different temperatures. (c) Superconducting transition under different magnetic fields. (d) Upper critical fields at different temperatures, and its fit by G–L relation.

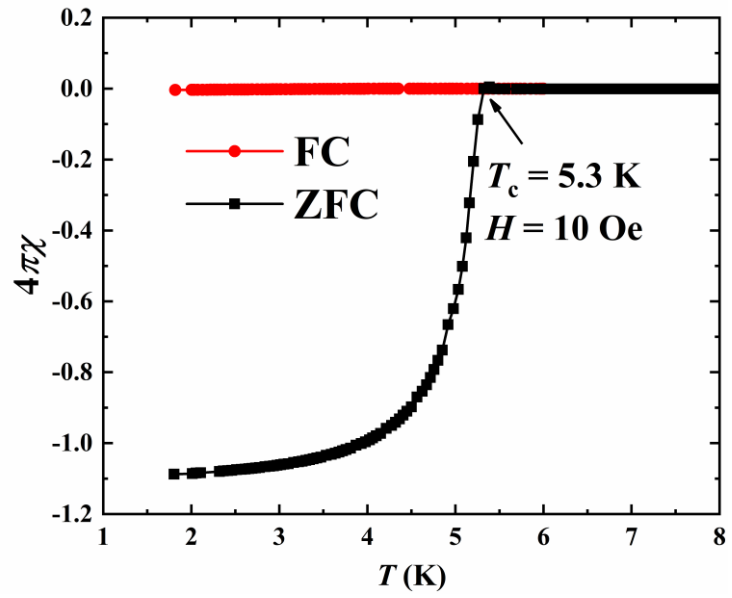

Figure S3: DC magnetic susceptibility of Ti_4Ir_2O prepared by arc-melting method.

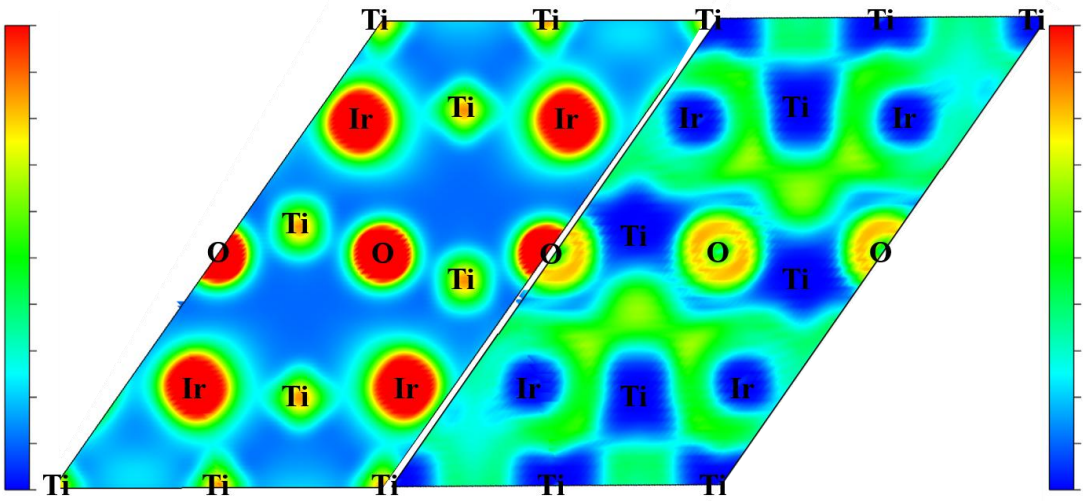

Figure S4: Charge density (left) and electron localization function (ELF) (right) of Ti_4Ir_2O calculated with SOC. The charge density is bound between 0 and 0.2 e/a_0^3 (a_0 is the Bohr radius), while ELF is bound between 0 and 1.

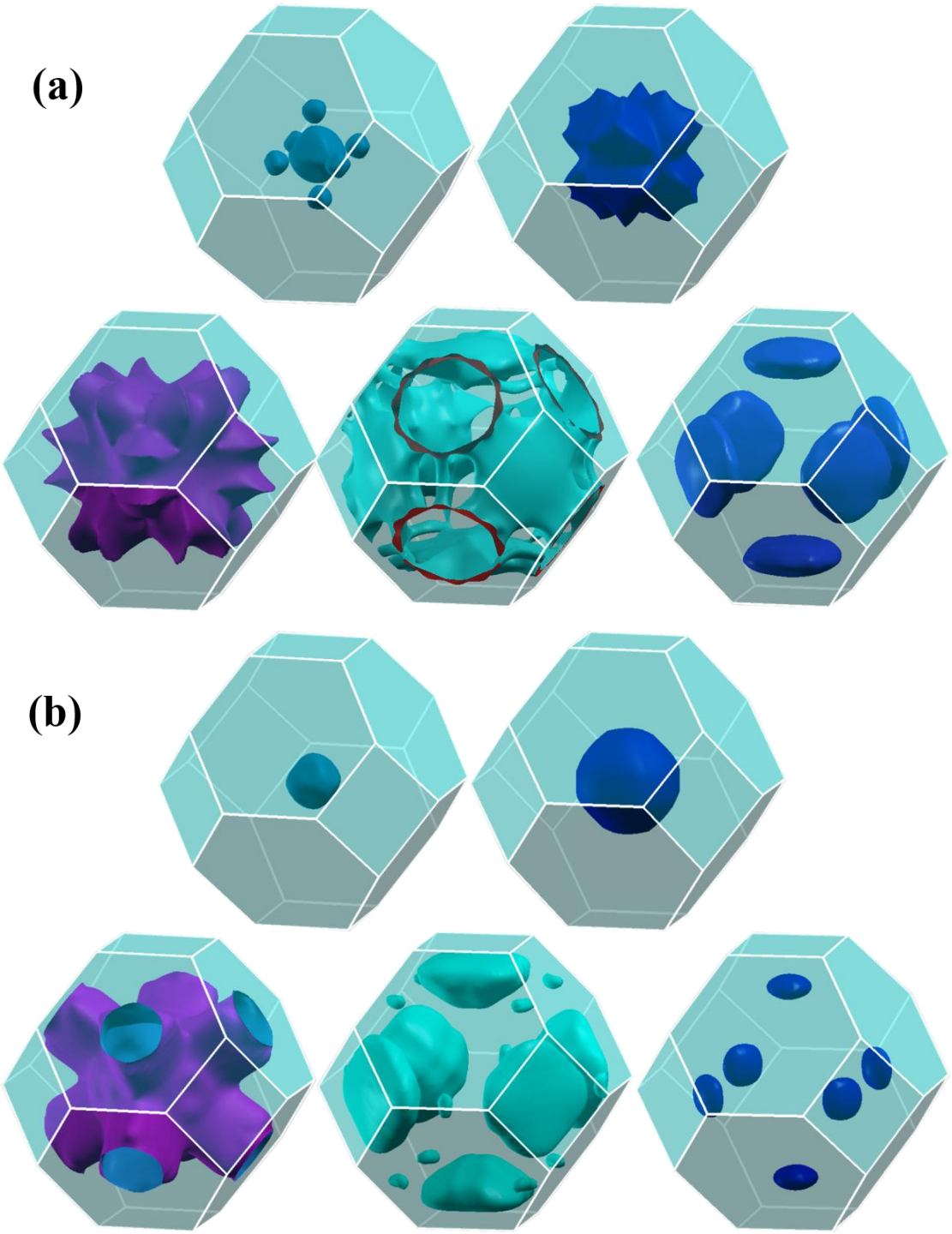

Figure S5: Fermi surfaces of Ti_4Ir_2O (a) without SOC and (b) with SOC.